

Reveal the large open-circuit voltage deficit of all-inorganic $CsPbIBr_2$ perovskite solar cells

Ying Hu(胡颖), Jiaping Wang(王家平), Peng Zhao(赵鹏), Zhenhua Lin(林珍华), Siyu Zhang(张思玉),Jie Su(苏杰), Miao Zhang(张苗), Jincheng Zhang(张进成), Jingjing Chang(常晶晶), and Yue Hao(郝跃)

Citation: Chin. Phys. B, 2022, 31 (**3**): 038804. DOI: 10.1088/1674-1056/ac464b
Journal homepage: http://cpb.iphy.ac.cn; http://iopscience.iop.org/cpb

What follows is a list of articles you may be interested in

Highly efficient bifacial semitransparent perovskite solar cells based on molecular doping of CuSCN hole transport layer

Shixin Hou(侯世欣), Biao Shi(石标), Pengyang Wang(王鹏阳), Yucheng Li(李玉成), Jie Zhang(张杰), Peirun Chen(陈沛润), Bingbing Chen(陈兵兵), Fuhua Hou(侯福华), Qian Huang(黄茜), Yi Ding(丁毅), Yuelong Li(李跃龙), Dekun Zhang(张德坤), Shengzhi Xu(许盛之), Ying Zhao(赵颖), Xiaodan Zhang(张晓丹)

Chin. Phys. B, 2020, 29 (**7**): 078801. DOI: 10.1088/1674-1056/ab99ae

Effect of carrier mobility on performance of perovskite solar cells

Yi-Fan Gu(顾一帆), Hui-Jing Du(杜会静), Nan-Nan Li(李楠楠), Lei Yang(杨蕾), Chun-Yu Zhou(周春宇)

Chin. Phys. B, 2019, 28 (**4**): 048802. DOI: 10.1088/1674-1056/28/4/048802

Efficient design of perovskite solar cell using mixed halide and copper oxide

Navneet kour, Rajesh Mehra, Chandni

Chin. Phys. B, 2018, 27 (**1**): 018801. DOI: 10.1088/1674-1056/27/1/018801

Simulation design of P-I-N-type all-perovskite solar cells with high efficiency

Hui-Jing Du(杜会静), Wei-Chao Wang(王韦超), Yi-Fan Gu(顾一帆)

Chin. Phys. B, 2017, 26 (**2**): 028803. DOI: 10.1088/1674-1056/26/2/028803

Device simulation of lead-free $CH_3NH_3SnI_3$ perovskite solar cells with high efficiency

Hui-Jing Du(杜会静), Wei-Chao Wang(王韦超), Jian-Zhuo Zhu(朱键卓)

Chin. Phys. B, 2016, 25 (**10**): 108802. DOI: 10.1088/1674-1056/25/10/108802

SPECIAL TOPIC — Emerging photovoltaic materials and devices

Reveal the large open-circuit voltage deficit of all-inorganic $CsPbIBr_2$ perovskite solar cells

Ying Hu(胡颖)[1,†], Jiaping Wang(王家平)[1,†], Peng Zhao(赵鹏)[1], Zhenhua Lin(林珍华)[1,‡], Siyu Zhang(张思玉)[1], Jie Su(苏杰)[1], Miao Zhang(张苗)[2], Jincheng Zhang(张进成)[1,2], Jingjing Chang(常晶晶)[1,2,§], and Yue Hao(郝跃)[1]

[1] *State Key Discipline Laboratory of Wide Band Gap Semiconductor Technology, School of Microelectronics, Xidian University, Xi'an* 710071, *China*
[2] *Advanced Interdisciplinary Research Center for Flexible Electronics, Xidian University, Xi'an* 710071, *China*

(Received 30 November 2021; revised manuscript received 20 December 2021; accepted manuscript online 24 December 2021)

Due to excellent thermal stability and optoelectronic properties, all-inorganic perovskite is one of the promising candidates to solve the thermal decomposition problem of conventional organic–inorganic hybrid perovskite solar cells (PSCs), but the larger voltage loss (V_{loss}) cannot be ignored, especially $CsPbIBr_2$, which limits the improvement of efficiency. To reduce V_{loss}, one promising solution is the modification of the energy level alignment between the perovskite layer and adjacent charge transport layer (CTL), which can facilitate charge extraction and reduce carrier recombination rate at the perovskite/CTL interface. Therefore, the key issues of minimum V_{loss} and high efficiency of $CsPbIBr_2$-based PSCs were studied in terms of the perovskite layer thickness, the effects of band offset of the CTL/perovskite layer, the doping concentration of the CTL, and the electrode work function in this study based on device simulations. The open-circuit voltage (V_{oc}) is increased from 1.37 V to 1.52 V by replacing SnO_2 with ZnO as the electron transport layer (ETL) due to more matching conduction band with the $CsPbIBr_2$ layer.

Keywords: all-inorganic perovskites, $CsPbIBr_2$ solar cells, device simulation, voltage loss, Silvaco TCAD

PACS: 88.40.H−, 88.40.hj, 88.40.fc **DOI:** 10.1088/1674-1056/ac464b

1. Introduction

Since Miyasaka *et al.* first employed perovskites as the photovoltaic absorber in 2009,[1] organic–inorganic lead halide perovskites have attracted great attention in photovoltaic applications. In recent years, the power conversion efficiency (PCE) of single-junction cells has been elevated to 25.5% closing to the Shockley–Queisser (S-Q) limit,[2,3] which is attributed to lots of researchers devoting to the exploration of perovskite solar cells (PSCs).[4–8] More importantly, the main reason for the success is that lead halide perovskites possess excellent optical and electrical properties, including tunable bandgap, high light absorption coefficient, low exciton binding energy, long carrier diffusion length, and long carrier lifetime.[5,8–15] However, conventional organic–inorganic hybrid PSCs contain organic cations, such as MA^+ and FA^+, which tend to evaporate and react with water molecules in the air and be easily decomposed by heat.[16–18] Considering superior thermal stability of perovskite material, the all-inorganic perovskites, such as $CsPbI_3$, $CsPbI_2Br$, $CsPbIBr_2$, $CsPbBr_3$, eliminate the organic components, which are the promising wide-bandgap candidates.[19–28] As the all-inorganic $CsPbI_3$ PSC was first reported by Snaith *et al.* with the PCE of 2.9%,[29] researchers have continuously improved the fabrication process of PSCs. In 2020, Sang Il Seok team reported a PCE of 20.37 % for all-inorganic PSCs, through adding a methylammonium chloride solution to accelerate the crystallization process of the all-inorganic perovskite, therefore the highly uniform and pinhole-minimized thin films were obtained, followed by surface passivation using octyl ammonium iodides in ambient air.[30] The highest PCE up to now for all-inorganic PSCs is 20.8%, since an environmentally benign material, histamine (HA), is designed to passivate the iodine vacancies in the perovskite thin film.[31] Yang *et al.* reported dye molecule-assisted engineering as interface passivation, thus reducing the interfacial charge recombination to obtain record-high open circuit voltage (V_{oc}) of 1.37 V and minimum voltage loss ($V_{loss} = E_g/q - V_{oc}$) of 0.68 V for $CsPbIBr_2$ (with a bandgap of 2.05 eV) PSCs, this V_{loss} is even higher than that of $CsPbBr_3$ (with a wider bandgap of 2.3 eV) PSCs.[19] At present, the highest reported V_{oc} of $CsPbBr_3$ PSCs is 1.70 V, corresponding to a minimum V_{loss} of 0.60 V.[32] Limited by severe V_{loss}, the current record-high PCE of $CsPbIBr_2$ PSCs is 11.04%, which is well below theoretical values of 21%.[33] Therefore, to further optimize the performance, theoretical analysis and research of $CsPbIBr_2$ PSCs V_{loss} should be carried out.

Generally speaking, minimizing the non-radiative recombination loss is vital to improve V_{oc} and reduce V_{loss}. Defects passivation of perovskite grain boundaries or film surface has been proved to be an effective measure to suppress the

[†]These authors contributed equally.
[‡]Corresponding author. E-mail: zhlin@xidian.edu.cn
[§]Corresponding author. E-mail: jjingchang@xidian.edu.cn

© 2022 Chinese Physical Society and IOP Publishing Ltd

non-radiative recombination.[19,34–38] In addition, the modification of the energy level alignment between perovskite layer and adjacent charge transport layer (CTL) can reduce charge recombination loss and facilitate charge extraction at perovskite/CTL interface.[39] In the following parts, $CsPbIBr_2$ PSC is employed to investigate the reasons for the high V_{loss}, and is expected to provide a guideline for designing high performance $CsPbIBr_2$ PSC with low V_{loss}. Firstly, the effect of the absorption layer thickness is studied comprehensively, and the optimal thickness is 200 nm. To achieve better energy level alignment, the influence of conduction and valence band offset is studied, and the V_{oc} of $CsPbIBr_2$ PSC with ZnO ETL is improved from 1.37 V to 1.52 V compared with SnO_2. In addition, the optimum doping concentrations of SnO_2 electron transport layer (ETL) and Spiro-OMeTAD hole transport layer (HTL) are 10^{19} cm^{-3} and 10^{21} cm^{-3}, respectively. Finally, the minimal V_{loss} and optimal performance are achieved when the cathode electrode work function is between −4.8 eV and −4.6 eV and the anode electrode work function is between −5.4 eV and −5.2 eV.

2. Method

In this study, optoelectronic simulator Silvaco TCAD is employed to optimize PSC. All-inorganic perovskite $CsPbIBr_2$ is used as the absorption layer. According to the existing reports, SnO_2 ETL and Spiro-OMeTAD (2,2′,7,7′-Tetrakis[N,N-di(4-methoxyphenyl)aMino]-9,9′-spirobifluorene) HTL in the $CsPbIBr_2$ PSC have the lowest V_{loss},[19] therefore, the planar device structure ITO/SnO_2/$CsPbIBr_2$/Spiro-OMeTAD/Ag is adopted in this study and shown in Fig. S1. Electrical parameters of the PSC are obtained from the literature and summarized in Table S1.[19,39–42] The theoretical analysis and simulation of PSCs are mainly based on the Poisson equation (Eq. (1)), carrier continuity (Eq. (2)), and drift-diffusion (Eq. (3));[43]

$$\frac{\partial^2\varphi}{\partial x^2} = \frac{q}{\varepsilon}(n-p), \tag{1}$$

$$\frac{\partial n}{\partial t} = \frac{1}{q}\frac{\partial J_n}{\partial x} + G - R, \quad \frac{\partial p}{\partial t} = \frac{1}{q}\frac{\partial J_p}{\partial x} + G - R, \tag{2}$$

$$J_n = qD_n\frac{\partial n}{\partial t} - q\mu_n n\frac{\partial \varphi}{\partial x}, \quad J_p = -qD_p\frac{\partial p}{\partial t} - q\mu_p p\frac{\partial \varphi}{\partial x}. \tag{3}$$

In addition, the Shockley–Read–Hall (SRH) recombination, Auger recombination and band-to-band recombination on device performance are considered in the simulation.[44,45] Moreover, the transfer-matrix method (TMM) is used as the optical model, in detail, the optical electric field can be calculated according to the following equations:

$$Q(x,\lambda) = \frac{2\pi c\varepsilon_0 kn|E(x)|^2}{\lambda}, \tag{4}$$

$$G(x) = \int_{\lambda_1}^{\lambda_2}\frac{\lambda}{hc}Q(x,\lambda)\,\mathrm{d}\lambda, \tag{5}$$

where ε_0 is the vacuum permittivity, c is the speed of light, n and k are the real and imaginary parts of the refractive index, respectively, $|E(x)|^2$ is the optical electric field, h is the Planck constant, λ is the wavelength, and $G(x)$ is the carrier generation rate. The refractive index n and extinction coefficient k of all-inorganic perovskites are obtained from the literature.[42,45] This work is simulated under the standard AM1.5G solar spectrum.

3. Results and discussion

3.1. Optimization of perovskite layer thickness

The perovskite absorption layer acts as the most important layer in PSC by absorbing light and converting into excitons or free carriers. Therefore, we first explored the influence of $CsPbIBr_2$ absorption layer thickness in this section. Figure 1(a) shows that short-circuit current density (J_{sc}) sharply increases when $CsPbIBr_2$ layer thickness is smaller than 100 nm, after that, the increase slows down and reaches saturation at 200 nm, and the saturation current is around 11.84 mA/cm^2. The V_{oc} decreases with the increase of the $CsPbIBr_2$ layer thickness. In addition, figures 1(c) and 1(d) show that the filling factor (FF) of the device almost remains unchanged, and PCE reaches saturation when the absorption layer thickness is 200 nm (J_{sc} is 11.83 mA/cm^2; V_{oc} is 1.53 V; FF is 85.19%; PCE is 15.53%). Therefore, in the following section, the solar cell with 200 nm $CsPbIBr_2$ layer is used as the standard device.

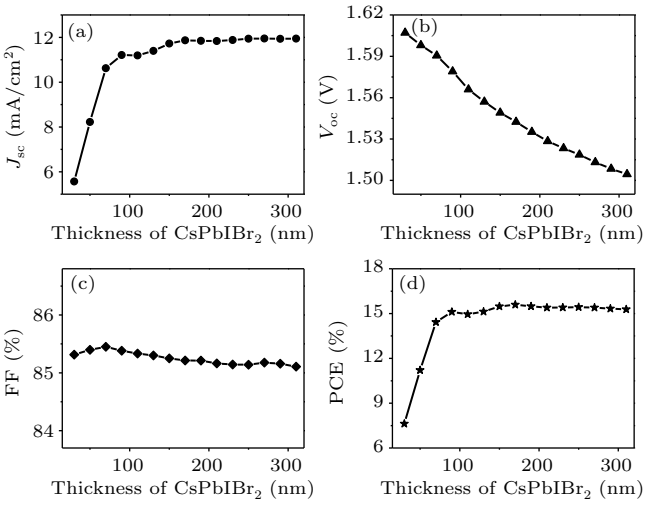


Fig. 1. Performance parameters of PSC device with different thickness of perovskite: (a) J_{sc}, (b) V_{oc}, (c) FF, and (d) PCE.

To further investigate the reasons for the trend of J_{sc}, the net carrier generation rate (the difference between the carrier generation rate and the carrier recombination rate) and external quantum efficiency (EQE) of different absorption layer thicknesses are simulated, as shown in Figs. 2(a) and 2(b), respectively. The net charge carrier generation rate increases with the increasing absorption layer thickness and tends to saturate at 200 nm, which is consistent with J_{sc}. According to

the EQE simulation results, with the perovskite layer thickness increasing from 50 nm to 300 nm, the EQE in short-wavelength region (< 400 nm) is almost unchanged, on the contrary, the EQE in long-wavelength region (> 400 nm) is significantly improved, which indicates that photons in the short-wavelength region (< 400 nm) can be almost completely absorbed by the thin perovskite film and the thickness increase mainly induces the improvement of photon absorption in the long-wavelength region (> 400 nm). Moreover, the situation of EQE is similar with that of J_{sc}.

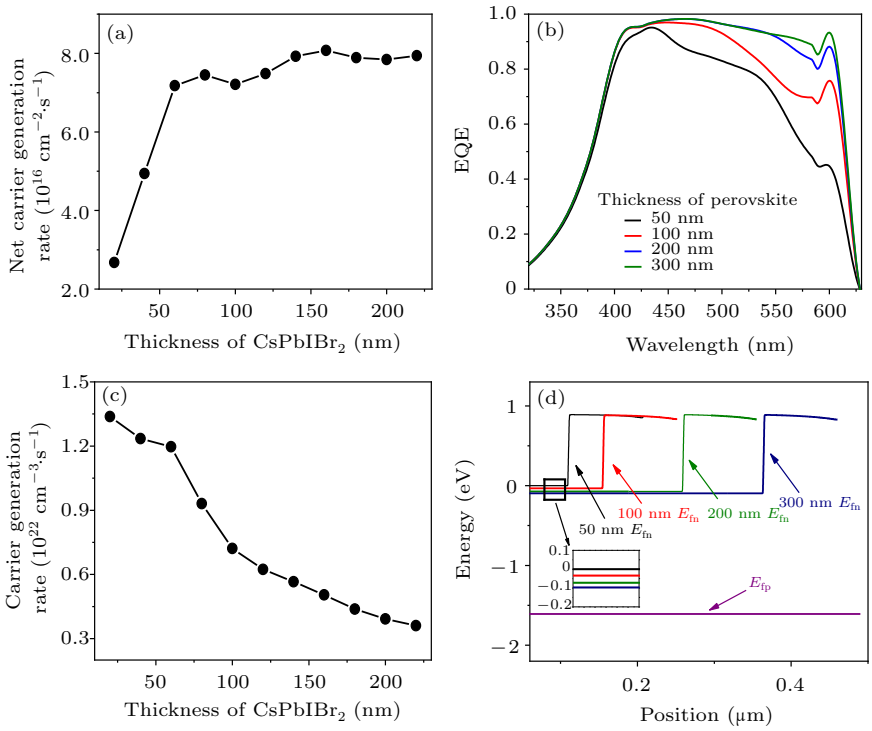


Fig. 2. (a) Net carrier generation rate and (b) EQE of PSCs with different thickness of perovskite layer. (c) Carrier generation rate and (d) energy band diagrams of the device with different perovskite layer thickness.

In order to further explore the V_{oc} variation, the carrier generation rate per unit thickness of the absorption layer is shown in Fig. 2(c) and exhibits an obvious declining trend, which indicates that the non-equilibrium carrier concentration reduces with the increase of the $CsPbIBr_2$ thickness. As we all know, electron quasi-Fermi level (E_{fn}) and hole quasi-Fermi level (E_{fp}) tend to close to each other due to the reduction of the non-equilibrium carrier concentration, in addition, V_{oc} is proportional to the difference between E_{fn} and E_{fp}. Therefore, the difference between E_{fn} and E_{fp} (Fig. 2(d)) decreases with the increase of the perovskite absorption layer thickness, which is the reason that V_{oc} keeps decreasing.

According to Eqs. (4) and (5), the photoelectric field of perovskite layers with different thickness is studied under the condition of 400 nm, 480 nm, 550 nm and 600 nm wavelengths respectively. Overall, the peak value of the photoelectric field increases with the wavelength from 400 nm to 550 nm, and then decreases at the wavelength of 600 nm. In Fig. 3(a), when the wavelength is 400 nm, the curves are almost overlapping, and the smooth descent of these curves indicates that there is no interference in the photoelectric field. Compared with the 400 nm wavelength, an obvious optical interference occurs when the wavelengths are 550 nm and 600 nm, as shown in Figs. 3(c) and 3(d). At the same wavelength, although the peak value of the photoelectric field decreases with the increase of the absorption layer thickness, the thicker absorber layer can continuously generate more carriers. These conclusions about the photoelectric field of various wavelengths are consistent with the EQE results in Fig. 2(b).

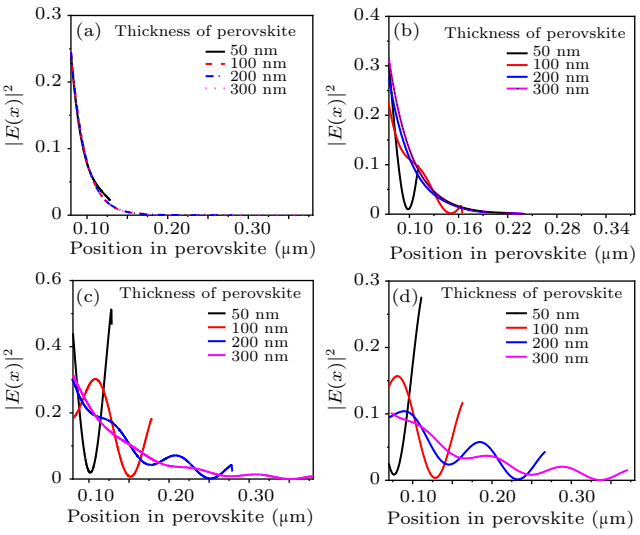


Fig. 3. Optical electric field ($|E(x)|^2$) of (a) 400 nm wavelength, (b) 480 nm wavelength, (c) 550 nm wavelength and (d) 600 nm wavelength.

3.2. Influence of conduction and valence band offset on device performance with interface defect layer

According to the previous research, the highest V_{oc} of the all-inorganic $CsPbIBr_2$ PSC is only 1.37 V,[19] which is far lower than the 1.53 V obtained by the standard device in this study. The high V_{loss} of the wide bandgap perovskite attributes to interface defects and band offset. Therefore, in this section, the influences of conduction band offset (CBO) and valence band offset (VBO) are studied. According to the literature,[46] we define 10 nm interface defect layer 1 (IDL1) and 2 (IDL2) at each of the interfaces of perovskite/ETL and perovskite/HTL, respectively.

3.2.1. Conduction band offset of perovskite/ETL layer

As shown in Fig. S2(a), when χ_{ETL} is greater than $\chi_{perovskite}$, which means that the conduction band (E_c) of perovskite is higher than that of ETL, CBO is set to be negative, and E_{c_IDL1} (E_{v_IDL1}) is set to be consistent with E_{c_ETL} ($E_{v_perovskite}$). As shown in Fig. S2(b), in the same way, when χ_{ETL} is smaller than $\chi_{perovskite}$, which means that $E_{c_perovskite}$ is lower than E_{c_ETL}, CBO is set to be positive, and E_{c_IDL1} and E_{v_IDL1} are set to be consistent with perovskite. The charge carrier lifetime of IDL1 is set to be 1 ns, other optical and electrical parameters are identical to those of the perovskite layer.

In Fig. 4(a), the J–V curves are almost overlapping when CBO increases from 0 to 0.5 eV, after that, when CBO exceeds 0.6 eV, J_{sc} and FF drop sharply. V_{oc} increases significantly when CBO increases from −0.6 eV to 0 eV. As shown in Fig. 4(b), there is a spike at the IDL1/ETL interface, and the barrier increases significantly when CBO exceeds 0.5 eV. Carrier transport from absorption layer to ETL is obviously impeded, resulting in the decline of J_{sc} and FF. As for V_{oc}, when CBO is −0.5 eV (Fig. 4(c)), the energy band diagram of PSCs shows that there is a cliff at the IDL1/perovskite interface. The cliff does not impede the electron transfer from perovskite to IDL1, however it leads to the increase of the carrier recombination rate in IDL1. In Fig. 4(d), the recombination rate reduces with the decrease of |CBO|. In addition, the spike impedes both photogeneration current (I_L) and the forward current (I_S), which leads to the decline of both I_L and I_S (Eq. (6)), therefore the V_{oc} remains constant at a fixed value when CBO is positive. In summary, when CBO is 0–0.5 eV, the optimal PCE (16.78%) of the device could be obtained.

$$V_{oc} = \frac{k_0 T}{q} \ln\left(\frac{I_L}{I_S} + 1\right). \tag{6}$$

The V_{oc} of the PSCs with SnO_2 ETL is only 1.37 V. The Cs-based PSCs with ZnO ETLs have been widely studied, and have achieved competitive efficiency and stability over those with other metal oxides in our previous study.[47] In order to obtain better device performance, ZnO ETL is investigated to suppress V_{loss} in PSCs. The material parameters of ZnO are obtained from the literature,[48] and the band diagram is shown in Fig. 5(a), it can be found that the conduction band of ZnO (CBO is −0.05 eV) is more suitable than that of SnO_2 (CBO is −0.3 eV). According to the result of the J–V curves in Fig. 5(b), the device performance with ZnO ETL is superior to that with SnO_2 ETL.

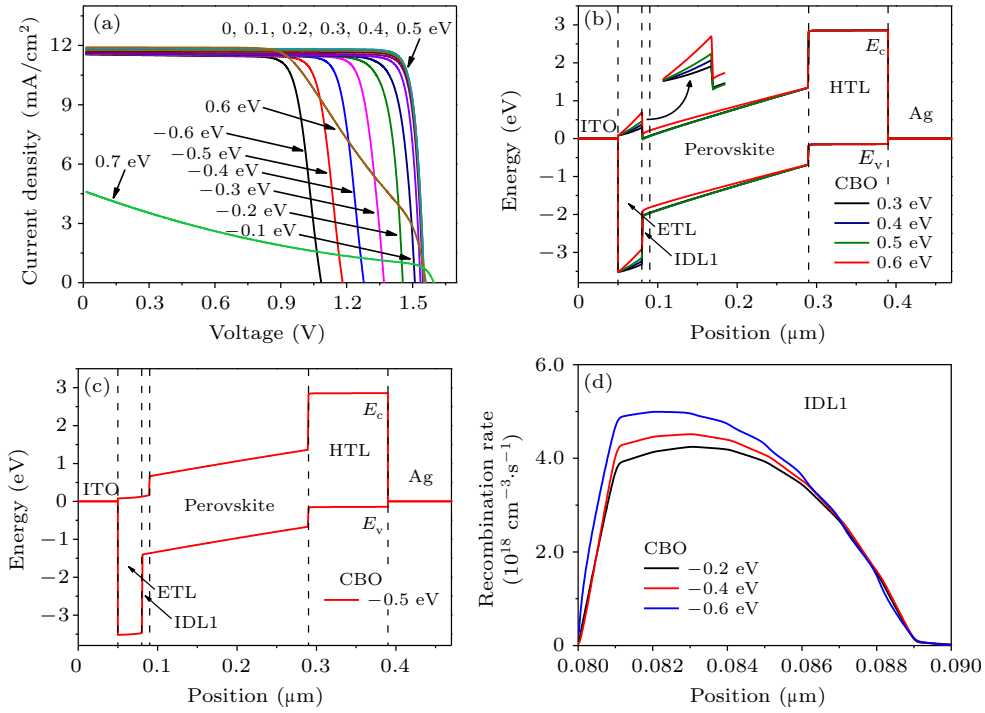


Fig. 4. (a) The J–V curves of the PSCs with different CBOs. (b) Energy band diagrams with the positive value of CBOs, and (c) energy band diagram with the negative value (−0.5 eV) of CBO. (d) Recombination rate in IDL1 of the device with different CBO.

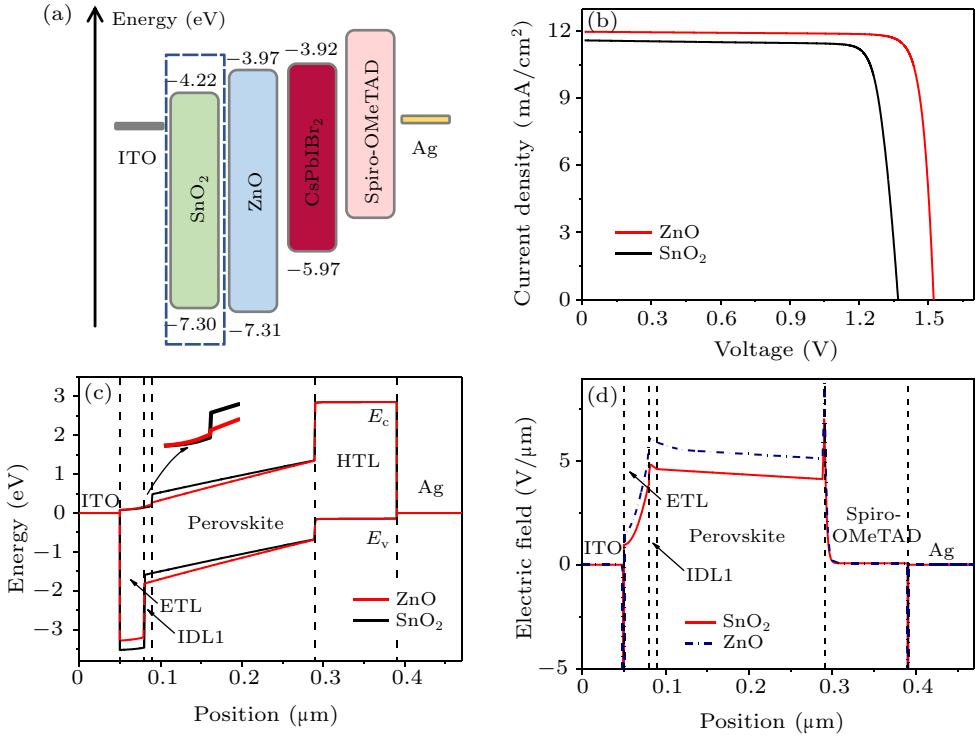


Fig. 5. (a) Energy band positions of the device. (b) The *J*–*V* curves, (c) energy band diagrams, (d) internal longitudinal electric field of the device with different CBO of PSCs with SnO_2 and ZnO as ETL, respectively.

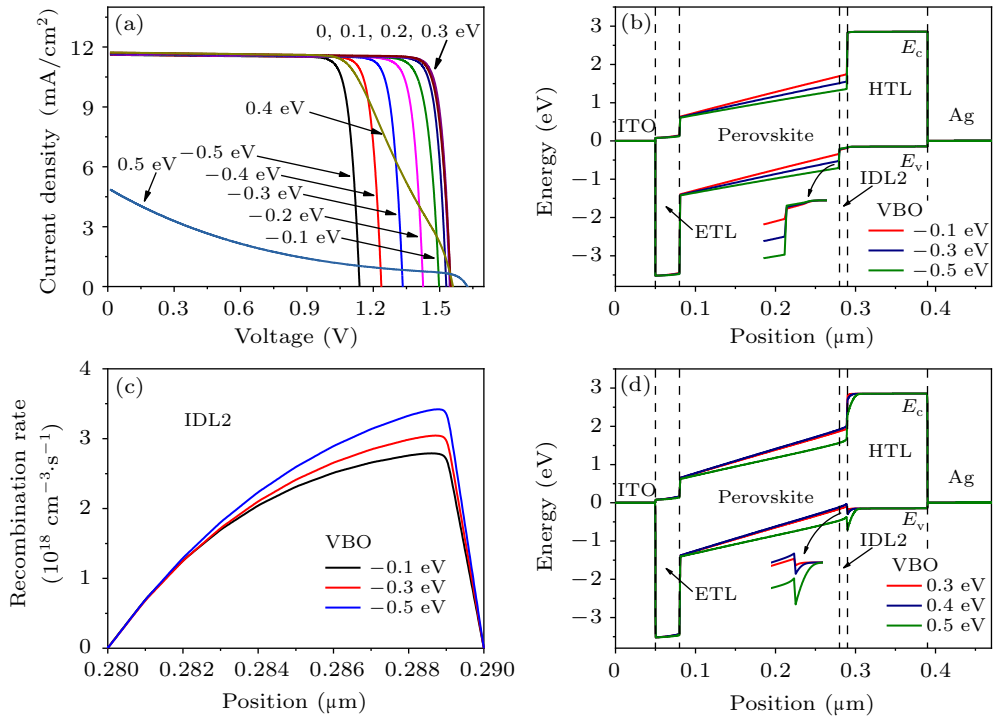


Fig. 6. (a) The *J*–*V* curves of the PSCs with different VBOs. (b) Energy band diagrams, and (c) recombination rate in IDL2 with the negative values of VBOs. (d) Energy band diagrams with the positive values of VBOs.

J_{sc} increases from 11.58 mA/cm^2 to 11.97 mA/cm^2, which attributes to the smaller parasitic absorption induced by the wider bandgap of ZnO. In addition, V_{oc} (FF) increases from 1.37 V (84.92%) to 1.52 V (87.91%). This is because there is no cliff based on ZnO ETL compared with SnO_2 ETL, as shown in Fig. 5(c), resulting in lower carrier recombination rate. Moreover, as shown in Fig. 5(d), the internal electric field with ZnO ETL is about 1 V/μm larger than that with SnO_2 ETL, which is conducive to the collection and extracting of carriers. Finally, the PCE of ZnO-based PSC (15.90%) is better than that of SnO_2-based PSC (13.47%). Consequently, the conduction band of ETL material should be more matching with that of perovskite in order to eliminate V_{loss} induced by CBO as much as possible.

3.2.2. Valence band offset of perovskite/HTL layer

As shown in Fig. S3(a), when E_{v_HTL} is greater than $E_{v_perovskite}$, VBO is set to be negative, and E_{v_IDL2} (E_{c_IDL2}) is set to be consistent with E_{v_HTL} ($E_{c_perovskite}$). In Fig. S3(b), when $E_{v_perovskite}$ is greater than E_{v_HTL}, VBO is set to be positive, and E_{c_IDL2} and E_{v_IDL2} are set to be consistent with perovskite. The charge carrier lifetime of IDL2 is set to be 1 ns, other optical and electrical parameters are identical to the perovskite layer.

As shown in Fig. 6(a), V_{oc} decreases obviously with the VBO declining from 0 to −0.5 eV. J_{sc} almost remains constant and FF decreases slightly. As shown in Fig. 6(b), when the VBO is negative, the cliff at the IDL2/perovskite interface rises with the raise of |VBO|, which leads to the increase of the carrier recombination rate in IDL2 (Fig. 6(c)). This explains the variation of performance parameters in Fig. 6(a). In addition, the device performance drops significantly when VBO is larger than 0.3 eV. A spike is formed at the IDL2/HTL interface (Fig. 6(d)), and the barrier increases significantly when VBO exceeds 0.3 eV. Carrier transport from absorption layer to HTL is seriously impeded, resulting in the decline of J_{sc} and FF. In addition, V_{oc} is almost constant when VBO is positive, and the reason is consistent with the analysis in the previous section. In summary, when VBO is 0–0.3 eV, the optimal PCE (16.09%) and minimum V_{loss} of the device could be obtained.

3.3. Optimization of doping concentration of charge transport layer

According to the previous reports, the doping of ETL could affect the extraction of free carriers and the device performance. The doping concentration of the ETL and HTL layer could be controlled by ion doping engineering approaches in experiments. In the simulation, doping concentrations of both ETL and HTL can be achieved by controlling the dopants type (donor concentration and acceptor concentration). The n-type doping concentration of the ETL layer is controlled and varied from 10^{15} cm^{-3} to 10^{21} cm^{-3} to study its influence on the performance in this work. As shown in Fig. 7, J_{sc} decreases slightly with the increase of SnO_2 doping concentration. The V_{oc} and FF increase firstly and then tend to saturate. The EQE almost remains constant with various ETL doping concentration (Fig. 8(a)), which indicates that the influence of the ETL doping concentration on light absorption is negligible.

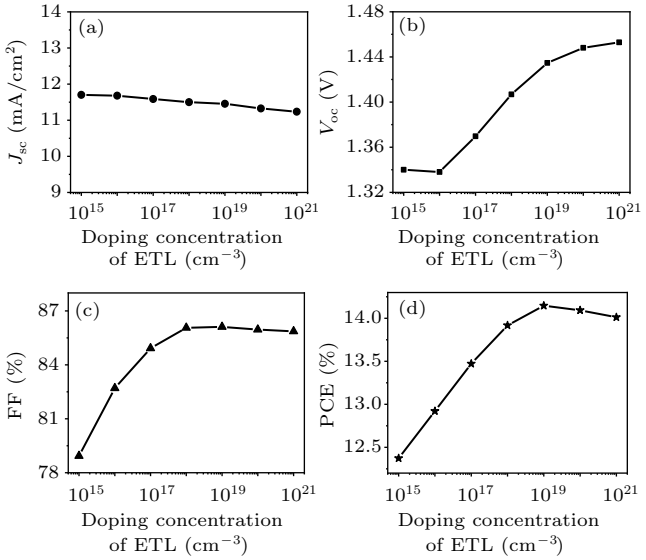


Fig. 7. Performance parameters of PSCs with different doping concentration of ETL: (a) J_{sc}, (b) V_{oc}, (c) FF, and (d) PCE.

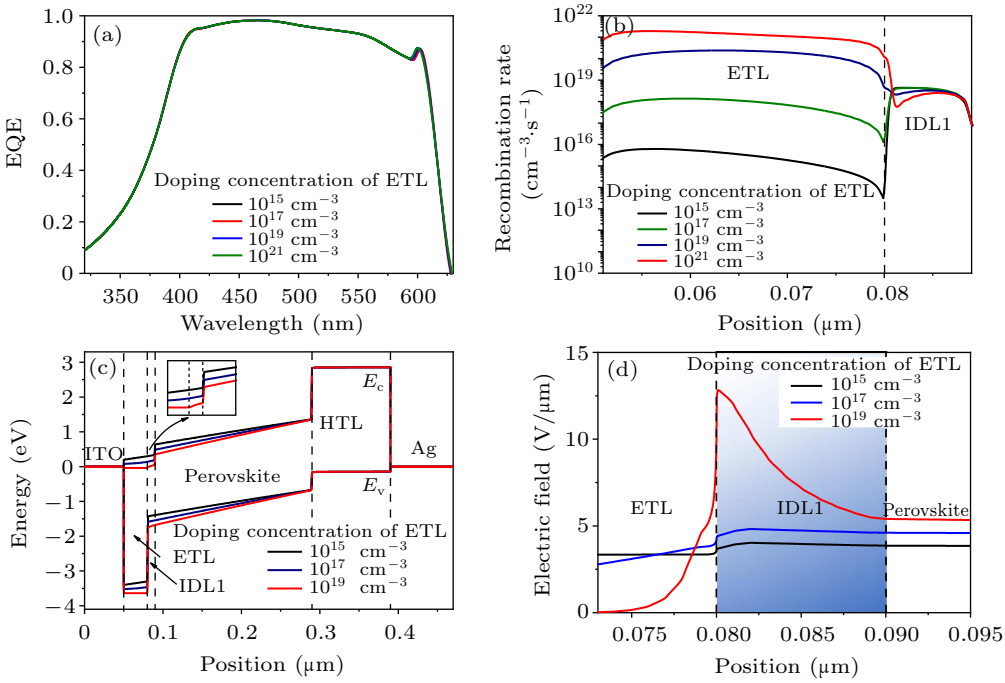


Fig. 8. (a) EQE, (b) recombination rate, (c) energy band diagrams, (d) internal longitudinal electric field with different doping concentration of ETL.

Figure 8(b) shows the carrier recombination rate in the SnO_2 layer. Impurity is a kind of recombination center, therefore the increase of doping concentration induces the reduction of carrier mobility, resulting in the increase of non-radiative recombination in ETL, leading to the decrease of J_{sc}. As shown in Fig. 8(c), the cliff does not change between the perovskite layer and IDL1 with the increase of SnO_2 doping concentration, therefore, the interface defect recombination rate is almost unchanged, however, the built-in electric fields in IDL1 and ETL significantly increase (Fig. 8(d)), so that the carriers can be collected more efficiently, this is consistent with the change of V_{oc} and FF. Finally, the optimal efficiency is 14.15% when the SnO_2 doping concentration is 10^{19} cm^3.

In addition, the different doping concentrations of Spiro-OMeTAD could affect V_{oc} and performance of PSCs as well. The p-type doping concentration of the HTL layer is varied from 10^{15} cm^{-3} to 10^{21} cm^{-3}. Figure 9(a) shows that J_{sc} decreases slightly with the increase of the Spiro-OMeTAD doping concentration, the main reason is that a large number of metal ions are added to produce the recombination center, which makes the non-radiative recombination in HTL increase sharply as shown in Fig. 10(a), leading to the decrease of J_{sc}. Moreover, figure 9(b) shows that V_{oc} increases significantly with the increase of the Spiro-OMeTAD doping concentration. The reason is, on the one hand, the energy band position is pulled higher with the increase of the Spiro-OMeTAD doping concentration (Fig. 10(b)), leading to the increase of the electric field in the interface defect layer IDL2, as shown in Fig. 10(c), so the carrier is extracted and separated efficiently by HTL. On the other hand, the cliff is unchanged, which results in that the interface defect recombination does not increase. Consequently, when the doping concentration of Spiro-OMeTAD is 10^{21} cm^{-3}, V_{oc} is improved from 1.14 V to 1.23 V effectively, and the optimal PCE is 12.04%.

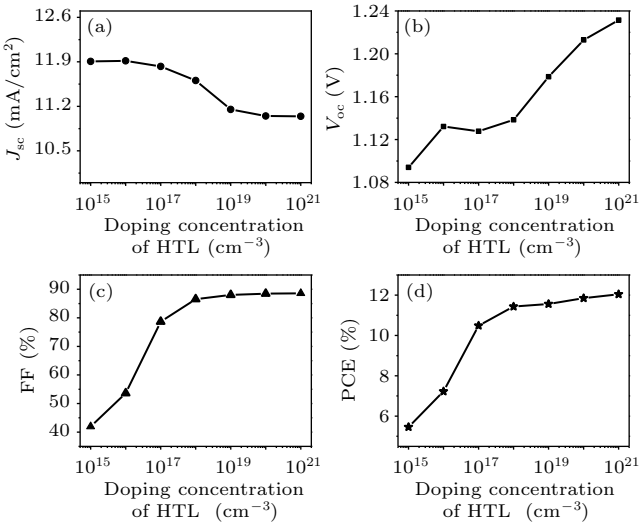


Fig. 9. Performance parameters of PSCs with different doping concentration of HTL: (a) J_{sc}, (b) V_{oc}, (c) FF, and (d) PCE.

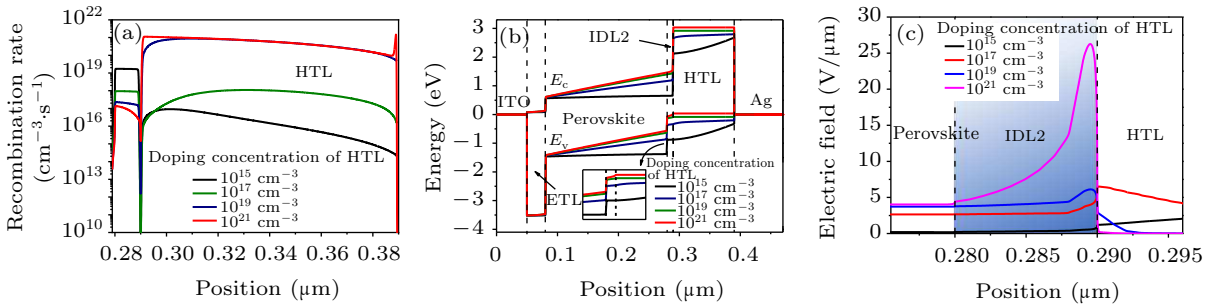


Fig. 10. (a) Recombination rate, (b) energy band diagrams (c) internal longitudinal electric field with different doping concentration of HTL.

3.4. Influence of electrode work function

In the above study, cathode and anode electrodes are set to ohmic contact. However, the Schottky contact between carrier transport layer and electrode could not be avoided, resulting in the change of the energy band diagrams. Thus, it is meaningful to explore the effect of cathode electrode work function ($\Phi_{cathode}$) and anode electrode work function (Φ_{anode}) on the performance of PSCs.

3.4.1. Influence of cathode electrode work function

In order to avoid the influence of Φ_{anode}, the contact between HTL and anode electrode is set to ohmic contact. By comparing J–V curves corresponding to different $\Phi_{cathode}$ from −4.8 eV to −6.2 eV (Fig. 11(a)), the device performance decreases significantly. As shown in Fig. 11(b), the conduction band of SnO_2 keeps elevating with the decrease of $\Phi_{cathode}$ from −4.8 eV to −6.2 eV, the slope of the energy band of the perovskite layer drastically reduces, which results in a significant decrease of the built-in electric field in the device, leading to the inefficient extraction of free carriers in the perovskite layer (Fig. 11(c)). Furthermore, a spike is formed in the energy band when $\Phi_{cathode}$ is between −5.4 eV and −6.2 eV, therefore, the negative electric field is generated inside the perovskite layer. This situation seriously hinders the transport of the carrier and results in the loss of the device performance. According to Figs. 11(d) and 11(e), the carrier concentration increases with the decrease of $\Phi_{cathode}$ from −4.8 eV to −5.4 eV, however, when $\Phi_{cathode}$ is between −5.8 eV and −6.2 eV, a large number of charge carriers cannot be efficiently collected by the corresponding

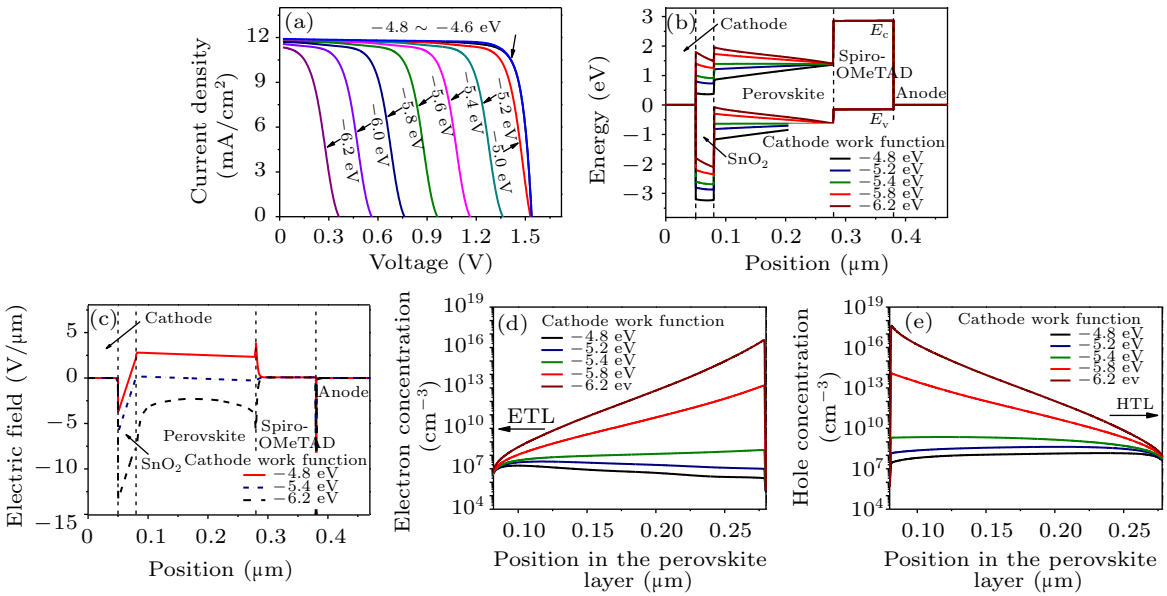


Fig. 11. (a) The *J*–*V* curves, (b) energy band diagrams and (c) internal longitudinal electric field of PSCs with different Φ_{cathode}. (d) Electron and (e) hole concentration distributions of the perovskite layer with various Φ_{cathode}.

charge transfer layer, resulting in the accumulation of carriers, which will lead to the increase of interface recombination and the loss of V_{oc}. In summary, the optimal performance of PSC ($J_{\text{sc}} = 11.86$ mA/cm^2, $V_{\text{oc}} = 1.54$ V, FF = 82.87%, PCE = 15.13%) can be obtained when Φ_{cathode} is between −4.8 eV and −4.6 eV. Generally speaking, transparent conductive oxide (TCO) film is used as cathode electrode in planar forward structure PSCs, Hence, ITO and FTO are suitable for the device structure in this study.

3.4.2. Influence of anode electrode work function

In this section, the contact between ETL and cathode electrode is set to ohmic contact. As shown in Fig. 12(a), the performance increases significantly with the decrease of Φ_{anode} from −4.0 eV to −5.4 eV. For planar forward structure PSCs, the anode electrode is usually made of metal. When the metal electrode is Schottky contact with the p-type semiconductor,

$$\Phi_{\text{B0}} = |E_{\text{v}}| - |\Phi_{\text{m}}|, \tag{7}$$

where Φ_{B0} is the barrier height of the metal–semiconductor contact, Φ_{m} is the metal work function, and E_{v} is the valence band of the semiconductor. Therefore, the closer the metal electrode work function and $E_{\text{v_Spiro-OMeTAD}}$ (−5.45 eV) are, resulting in a smaller barrier, the easier hole tunneling will be. As shown in Figs. 12(b) and 12(c), the energy band of Spiro-OMeTAD is pulled up with the drop of Φ_{anode},

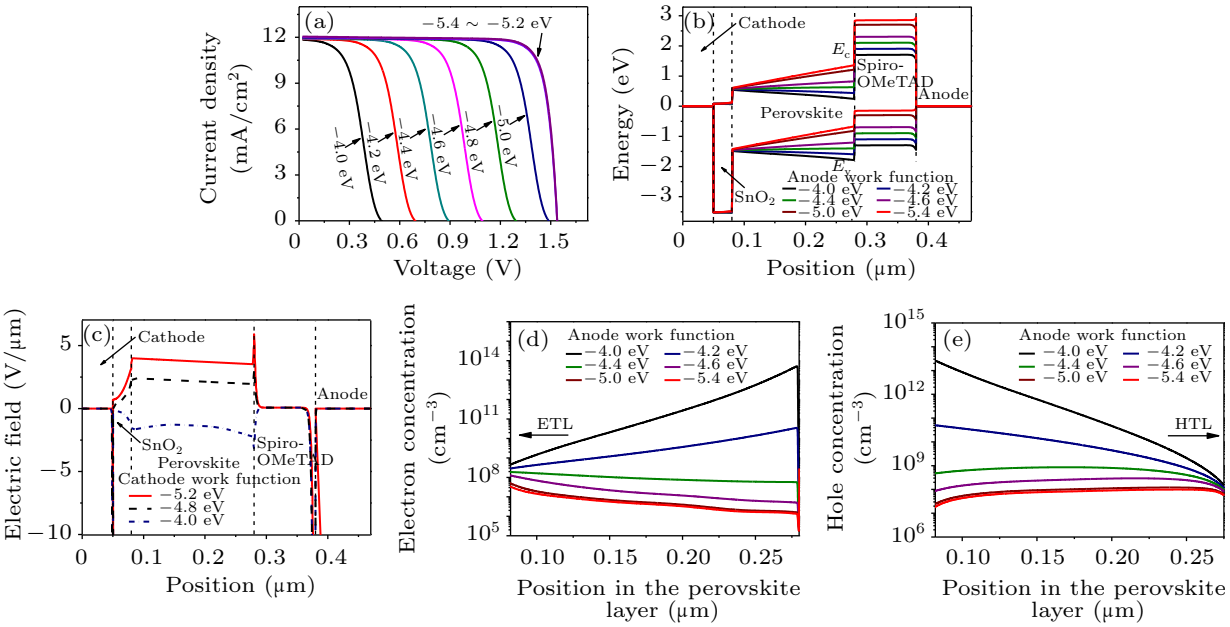


Fig. 12. (a) The *J*–*V* curves, (b) energy band diagrams and (c) internal longitudinal electric field of PSCs with different Φ_{anode}. (d) Electron and (e) hole concentration distributions of the perovskite layer with various Φ_{anode}.

therefore the energy band slope of the perovskite layer increases, leading to a significant increase of the built-in electric field. Figures 12(d) and 12(e) show that the carrier concentration in the absorption layer decreases continuously with the decrease of Φ_{anode}, indicating that the non-equilibrium carriers are effectively collected by CTL. However, the higher Φ_{anode} will cause the accumulation of carriers on both sides of the perovskite layer and lead to the loss of V_{oc}. In summary, V_{loss} is minimum when Φ_{anode} is between −5.4 eV and −5.2 eV, and the optimal performance ($J_{sc} = 12.05$ mA/cm^2, $V_{oc} = 1.54$ V, FF = 83.20%, PCE = 15.44%) is obtained. Au ($\Phi_m = -5.1$ eV) is a suitable anode electrode material.

4. Conclusion

Several factors that affect the V_{oc} and the performance of single-junction $CsPbIBr_2$ PSC are investigated. Firstly, the thickness of the absorption layer is studied and the optimal value is 200 nm. As for CBO, when the conduction band of perovskite is higher than that of ETL, the band cliff leads to the increase of the carrier recombination rate in the interface defect layer, and V_{loss} increases obviously. In contrast, when the conduction band of perovskite is lower than that of ETL, the spike seriously hinders the transport of carriers from the absorber layer to ETL, resulting in the decrease of J_{sc} and FF, however, there is almost no influence on V_{oc} due to the decrease of both the photoelectric current and the forward current. The suitable value of CBO is 0–0.5 eV, and the V_{oc} of $CsPbIBr_2$ PSC with ZnO ETL increases significantly from 1.37 V to 1.52 V compared with that with SnO_2 ETL, owing to the better matching conduction band with $CsPbIBr_2$ absorption layer. The optimum VBO is 0–0.3 eV, and the reason is similar to CBO. What's more, the doping concentration of CTL is optimized to minimize V_{loss} and improve the performance. The optimum doping concentrations of SnO_2 and Spiro-OMeTAD are 10^{19} cm^{-3} and 10^{21} cm^{-3}, respectively. Finally, when $\Phi_{cathode}$ (Φ_{anode}) is between −4.8 eV and −4.6 eV (between −5.4 eV and −5.2 eV), the minimal V_{loss} and optimal performance are obtained.

Acknowledgements

This work was financially supported by the National Natural Science Foundation of China (Grant No. 52192610), the Key Research and Development Program of Shaanxi Province, China (Grant No. 2020GY-310), Youth Project of Natural Science Basic Research Program of Shaanxi Province, China (Grant No. 2021JQ-189), the Joint Research Funds of Department of Science & Technology of Shaanxi Province and Northwestern Polytechnical University (Grant No. 2020GXLH-Z-018), and the Fundamental Research Funds for the Central Universities, China.

References

[1] Kojima A, Teshima K, Shirai Y and Miyasaka T 2009 *J. Am. Chem. Soc.* **131** 6050
[2] NREL 2020 *Best Research-Cell Efficiency Chart* (accessed: May 2020)
[3] Sha W E I, Ren X, Chen L and Choy W C H 2015 *Appl. Phys. Lett.* **106** 221104
[4] Shen W, Dong Y, Huang F, Cheng Y B and Zhong J 2021 *Mater. Reports: Energy* **1** 100060
[5] Chang J, Lin Z, Zhu H, Isikgor F H, Xu Q H, Zhang C, Hao Y and Ouyang J 2016 *J. Mater. Chem. A* **4** 16546
[6] Liu Z, Chang J, Lin Z, Zhou L, Yang Z, Chen D, Zhang C, Liu S F and Hao Y 2018 *Adv. Energy Mater.* **8** 1703432
[7] Zhou L, Lin Z, Ning Z, Li T, Guo X, Ma J, Su J, Zhang C, Zhang J, Liu S, Chang J and Hao Y 2019 *Sol. RRL* **3** 1900293
[8] Zhang B, Su J, Guo X, Zhou L, Lin Z, Feng L, Zhang J, Chang J and Hao Y 2020 *Adv. Sci.* **7** 1903044
[9] Yang J, Zhang P, Wang J and Wei S H 2020 *Chin. Phys. B* **29** 108401
[10] Jesper Jacobsson T, Correa-Baena J P, Pazoki M, Saliba M, Schenk K, Grätzel M and Hagfeldt A 2016 *Energy Environ. Sci.* **9** 1706
[11] Liu L, Lu J, Wang H, Cui Z, Giorgi G, Bai Y and Chen Q 2021 *Mater. Reports Energy* **1** 100064
[12] Zeng Q, Zhang X, Feng X, Lu S, Chen Z, Yong X, Redfern S A T, Wei H, Wang H, Shen H, Zhang W, Zheng W, Zhang H, Tse J S and Yang B 2018 *Adv. Mater.* **30** 1705393
[13] Chang J, Zhu H, Li B, Isikgor F H, Hao Y, Xu Q and Ouyang J 2016 *J. Mater. Chem. A* **4** 887
[14] Di J, Chang J and Liu S (Frank) 2020 *EcoMat* **2** e12036
[15] Di J, Du J, Lin Z, Liu S Frank, Ouyang J and Chang J 2021 *InfoMat* **3** 293
[16] Correa-Baena J P, Saliba M, Buonassisi T, Grätzel M, Abate A, Tress W and Hagfeldt A 2017 *Science* **358** 739
[17] Gao L, Spanopoulos I, Ke W, Huang S, Hadar I, Chen L, Li X, Yang G and Kanatzidis M G 2019 *ACS Energy Lett.* **4** 1763
[18] Tang S, Deng Y, Zheng X, Bai Y, Fang Y, Dong Q, Wei H and Huang J 2017 *Adv. Energy Mater.* **7** 1700302
[19] Yang S, Guo Z, Gao L, Yu F, Zhang C, Fan M, Wei G and Ma T 2019 *Sol. RRL* **3** 1900212
[20] Guo Z, Jena A K, Takei I, Kim G M, Kamarudin M A, Sanehira Y, Ishii A, Numata Y, Hayase S and Miyasaka T 2020 *J. Am. Chem. Soc.* **142** 9725
[21] Zhu J, Tang M, He B, Zhang W, Li X, Gong Z, Chen H, Duan Y and Tang Q 2020 *J. Mater. Chem. A* **8** 20987
[22] Yuan J, Ling X, Yang D, Li F, Zhou S, Shi J, Qian Y, Hu J, Sun Y, Yang Y, Gao X, Duhm S, Zhang Q and Ma W 2018 *Joule* **2** 2450
[23] Di J, Li H, Su J, Yuan H, Lin Z, Zhao K, Chang J and Hao Y 2021 *Adv. Sci.* **8** 2103482
[24] Ma J, Lin Z, Guo X, Zhou L, He J, Yang Z, Zhang J, Hao Y, Liu S and Chang J 2021 *J. Energy Chem.* **63** 558
[25] He J, Su J, Lin Z, Ma J, Zhou L, Zhang S, Liu S, Chang J and Hao Y 2021 *Adv. Sci.* **8** 2101367
[26] Guo Y, Su J, Wang L, Lin Z, Hao Y and Chang J 2021 *J. Phys. Chem. Lett.* **12** 3393
[27] Wang L, Su J, Guo Y, Lin Z, Hao Y and Chang J 2021 *J. Phys. Chem. Lett.* **12** 1098
[28] Ma J, Su J, Lin Z, He J, Zhou L, Li T, Zhang J, Liu S, Chang J and Hao Y 2021 *Energy Environ. Mater.* eem2.12212
[29] Eperon G E, Paternò G M, Sutton R J, Zampetti A, Haghighirad A A, Cacialli F and Snaith H J 2015 *J. Mater. Chem. A* **3** 19688
[30] Yoon S M, Min H, Kim J B, Kim G, Lee K S and Seok S Il 2021 *Joule* **5** 183
[31] Gu X, Xiang W, Tian Q and Liu S (Frank) 2021 *Angew. Chemie Int. Ed.* **60** 23164
[32] Zhou Q, Duan J, Yang X, Duan Y and Tang Q 2020 *Angew. Chemie Int. Ed.* **132** 22181
[33] Duan J, Xu H, Sha W E I, Zhao Y, Wang Y, Yang X and Tang Q 2019 *J. Mater. Chem. A* **7** 21036
[34] Jiang Q, Zhao Y, Zhang X, Yang X, Chen Y, Chu Z, Ye Q, Li X, Yin Z and You J 2019 *Nat. Photon.* **13** 460
[35] Jeon N J, Na H, Jung E H, Yang T Y, Lee Y G, Kim G, Shin H W, Il Seok S, Lee J and Seo J 2018 *Nat. Energy* **3** 682
[36] Liu C, Zeng Q and Yang B 2019 *Adv. Mater. Interfaces* **6** 1901136

[37] Zhou L, Su J, Lin Z, Guo X, Ma J, Li T, Zhang J, Chang J and Hao Y 2021 *Research* **2021** 9836752
[38] Guo X, Su J, Lin Z, Wang X, Wang Q, Zeng Z, Chang J and Hao Y 2021 *iScience* **24** 102276
[39] Zhang C, Lu Y N, Wu W Q and Wang L 2021 *Nano Energy* **81** 105634
[40] Bian H, Bai D, Jin Z, Wang K, Liang L, Wang H, Zhang J, Wang Q and Liu S (Frank) 2018 *Joule* **2** 1500
[41] Han Y, Meyer S, Dkhissi Y, Weber K, Pringle J M, Bach U, Spiccia L and Cheng Y B 2015 *J. Mater. Chem. A* **3** 8139
[42] Zhao P, Su J, Guo Y, Wang L, Lin Z, Zhang J, Hao Y, Ouyang X and Chang J 2021 *Mater. Today Phys.* **20** 100446
[43] Zhao P, Liu Z, Lin Z, Chen D, Su J, Zhang C, Zhang J, Chang J and Hao Y 2018 *Sol. Energy* **169** 11
[44] Zhao P, Su J, Lin Z, Wang J, Zhang J, Hao Y, Ouyang X and Chang J 2020 *Mater. Today Energy* **17** 100481
[45] Zhao P, Lin Z, Wang J, Yue M, Su J, Zhang J, Chang J and Hao Y 2019 *ACS Appl. Energy Mater.* **2** 4504
[46] Minemoto T and Julayhi J 2013 *Curr. Appl. Phys.* **13** 103
[47] Ma J, Su J, Lin Z, Zhou L, He J, Zhang J, Liu S, Chang J and Hao Y 2020 *Nano Energy* **67** 104241
[48] Yue M, Su J, Zhao P, Lin Z, Zhang J, Chang J and Hao Y 2019 *Nano-Micro Lett.* **11** 91